Equivalent Area Targets for Inverse Design Optimization With Changing Low-Boom Cruise Conditions

Wu Li*
NASA Langley Research Center, Hampton, Virginia 23681, USA

This paper provides theoretical and numerical justifications for inverse design optimization of reversed equivalent area ($A_{e,r}$) of low-boom supersonic aircraft when the cruise condition changes during the optimization iterations. A modified linear theory for steady flow around a supersonic projectile is used to establish the accuracy of $A_{e,r}$-based body-of-revolution approximation of a low-boom supersonic aircraft for undertrack sonic boom analysis using computational fluid dynamics off-body pressure. As a result, designing a low-boom shape of the off-body pressure at three body lengths below the aircraft is equivalent to designing a low-boom $A_{e,r}$ shape. A Bezier curve with eight control points is used to define an $A_{e,r}$ target for inverse design optimization of $A_{e,r}$ of a supersonic aircraft. To make an $A_{e,r}$ target matchable by a low-boom supersonic aircraft, the $A_{e,r}$ target must have the minimal perceived level of decibels (PLdB) for sonic boom and satisfy two constraints defined by the cruise condition, effective length, and two nondimensional parameters. Numerical results are used to verify that, for different cruise conditions, all optimized $A_{e,r}$ targets with PLdB below 70 can be approximately generated by scaling one of them if the targets have the same nondimensional parameters and approximately the same effective length.

Nomenclature

A_e	=	any equivalent area including $A_{e,m}$, $A_{e,CFD}$, and $A_{e,r}$, ft^2
$A_e(\boldsymbol{D})$, $A_e(\boldsymbol{D}_0)$	=	A_e for $\boldsymbol{D}$ or $\boldsymbol{D}_0$, ft^2
$A_e(x_e)$	=	value of A_e at effective distance location x_e, ft^2
A'_e	=	first derivative of A_e with respect to x_e
A''_e	=	second derivative of A_e with respect to x_e
$A_{e,CFD}$	=	$A_{e,m}$ calculated using volume and lift distributions from computational fluid dynamics analysis, ft^2
$A_{e,m}$	=	equivalent area defined by Mach angle cut method, ft^2
$A_{e,m}(l_e,\boldsymbol{C})$	=	value of $A_{e,m}$ at l_e that is determined by cruise condition $\boldsymbol{C}$, ft^2
$A_{e,r}$	=	reversed equivalent area defined by using reverse propagation of computational fluid dynamics off-body pressure, ft^2
$A_{e,r}^{opt}$	=	$A_{e,r}$ target optimized for lowest perceived level in decibels of undertrack ground signature, ft^2
$A_{e,r}^{opt}(\boldsymbol{C},l_e)$	=	$A_{e,r}^{opt}$ generated for $\boldsymbol{C}$ and l_e, ft^2
$A_{e,r}^{opt}(x_e,\boldsymbol{C},l_e)$	=	value of $A_{e,r}^{opt}(\boldsymbol{C},l_e)$ at x_e, ft^2
$A_{e,r,0}^{opt}$	=	nondimensional form of $A_{e,r}^{opt}$
$A_{e,r}^{target}(\boldsymbol{C},l_e)$	=	scaled $A_{e,r}$ target for $\boldsymbol{C}$ and l_e, ft^2
$A_{e,r}^{target}(x_e,\boldsymbol{C},l_e)$	=	value of $A_{e,r}^{target}(\boldsymbol{C},l_e)$ at x_e, ft^2
$\boldsymbol{B}_r$	=	body of revolution with its $A_{e,m}$ matching $A_{e,r}$ of a supersonic aircraft
$\boldsymbol{C}$	=	vector of cruise condition parameters (M, H, W_{crs})
$\boldsymbol{C}_i$	=	specific instance of $\boldsymbol{C}$ (i = 0, 1, and 2)
$\boldsymbol{D}$, $\boldsymbol{D}_0$	=	notations to represent supersonic configurations
$\widehat{\boldsymbol{D}}_{MaxR}$	=	notation for a low-boom design in a reference paper
dp/p	=	nondimensional overpressure $(p - p_\infty)/p_\infty$
$\boldsymbol{d}_{tgt}$	=	vector of (x,y) coordinates of 6 control points of Bezier curve
$F(t)$	=	F-function for A_e
$F_r(t)$	=	F-function for $A_{e,r}$

* Senior Research Engineer, Aeronautics Systems Analysis Branch

h = distance from undertrack location to aircraft, ft
h_0 = value of h fixed at 50 ft
H = cruise altitude for sonic boom analysis, ft
l_e = effective length of supersonic configuration, which is the largest effective distance where Mach angle cut plane intersects the configuration, ft
$l_{e,0}$ = l_e of a baseline configuration at cruise condition $\boldsymbol{C}_0$, ft
M = cruise Mach
p = longitudinal pressure distribution at undertrack location below aircraft, lb/ft^2
$p(x, \boldsymbol{B}_r)$ = longitudinal pressure distribution of $\boldsymbol{B}_r$ at undertrack location evaluated at x, lb/ft^2
p_r = pressure distribution obtained from reverse propagation of p, lb/ft^2
p_∞ = ambient pressure, lb/ft^2
PLdB(A_e) = perceived level in decibels of undertrack ground signature for A_e
t = independent variable
U_∞ = freestream velocity at cruise altitude H, ft/sec
W_{crs} = cruise weight for sonic boom analysis, lb
x, y, z = coordinates of point in space, ft
$x_{c,i}, y_{c,i}$ = (x,y) coordinates of control point for Bezier curve, ft
x_e = effective distance for A_e, ft
x_{frt} = effective distance location for leading edge of root airfoil of the most forward lifting surface, ft
β = Prandtl-Glauert factor $\sqrt{M^2-1}$
γ = ratio of specific heats
δ = lower bound for trim ratio $A_{e,r}^{opt}(l_e/2)/A_{e,r}^{opt}(l_e)$
μ = an a priori estimate of $A_{e,r}(l_e)/A_{e,CFD}(l_e)$ for expected low-boom design
ρ_∞ = ambient density at cruise altitude H, lb/ft^3

I. Introduction

DESIGN of low-boom supersonic aircraft requires multidisciplinary optimization (MDO) to satisfy both low-boom and mission requirements. For perceived level in decibels (PLdB) [1] of sonic boom as a low-boom design objective, only inverse design optimization methods [2-6] using computational fluid dynamics (CFD) analysis are effective to attain low-boom configurations with ground noise levels below 79 PLdB. Integration of CFD-based low-boom inverse design optimization and mission performance optimization can help develop supersonic aircraft satisfying both low-boom and mission requirements. A CFD-based multiobjective MDO problem with low-boom inverse design constraints was successfully solved using a block coordinate optimization (BCO) method [7]. The generated low-boom supersonic aircraft concept carries 40 passengers at seat pitch of 48 in, flies a low-boom overland mission with cruise Mach of 1.7 and range of 3500 nm, cruises overwater at Mach 1.8 with range of 3882 nm, and satisfies the takeoff and landing constraints. At the start of low-boom cruise, this low-boom concept has a reversed equivalent area ($A_{e,r}$) [3] closely matching an $A_{e,r}$ target with undertrack ground noise level of 69.9 PLdB, can be trimmed with an Euler CFD trim margin of 1.9 ft using fuel redistribution, and has an inviscid lift-to-drag ratio of 10.1 and a low-fidelity lift-to-drag ratio (including the skin friction drag) of 7.7. Here the trim margin is defined as the difference of the longitudinal center of pressure (CP) and the most aft longitudinal center of gravity (CG). An appropriate trim margin allows the supersonic aircraft to be trimmed with fuel redistributions instead of control surface deflections, so the aircraft can maintain the designed low-boom shape during the cruise flight.

The BCO method simultaneously minimizes an inverse design objective for $A_{e,r}$ to attain a low-boom aircraft shape and optimizes mission performance metrics (such as the takeoff gross weight and range). This requires the $A_{e,r}$ target for inverse design optimization to change with the low-boom cruise condition (M, H, W_{crs}) during low-boom MDO. So, the BCO method scales one optimized $A_{e,r}$ target for the low-boom cruise condition of a baseline configuration to generate the $A_{e,r}$ targets for different cruise conditions {see eq. (9) in Ref. [7]}. This solution method implicitly assumes that the scaled $A_{e,r}$ targets are approximately optimal for the designs generated during the BCO iterations.

This paper aims to answer a theoretical question for coupling the low-boom inverse design optimization of $A_{e,r}$ with the mission performance optimization—how the optimal $A_{e,r}$ target for low-boom inverse design optimization changes as the low-boom cruise condition varies with the weight at the start of cruise. (Note that the aircraft weight at the start of cruise changes as the design is modified by the mission performance optimization.) The key contribution is to numerically verify that, for different cruise conditions and $A_{e,r}$ targets defined by Bezier curves, all $A_{e,r}$ targets optimized for PLdB can be approximately generated by scaling one of them under some constraints. The numerical

results confirm that the low-boom design generated by the BCO method [7] has approximately the optimal low-boom $A_{e,r}$ shape at the start of low-boom cruise.

The paper is organized as follows. To lay the theoretical foundation for low-boom inverse design optimization of $A_{e,r}$, the body-of-revolution (BOR) approximation theory using $A_{e,r}$ is developed in Sec. II. Whitham's modified linear theory [8] for steady flow around a supersonic projectile is used to verify the accuracy of $A_{e,r}$-based BOR approximation of a low-boom supersonic aircraft for undertrack sonic boom analysis using CFD off-body pressure. Section III contains numerical results for verification of approximate optimality of the scaled $A_{e,r}$ targets for different cruise conditions. The last section has the conclusions.

II. BOR Approximation of Supersonic Aircraft

This section provides a theoretical justification of why the BOR defined by $A_{e,r}$ of a low-boom supersonic aircraft is a good approximation of the aircraft for undertrack sonic boom analysis using CFD off-body pressure. The justification starts with Whitham's modified linear theory [8] for steady flow around a supersonic projectile. Whitham introduced the F-function of the equivalent area $A_{e,m}$ of a supersonic projectile for prediction of the pressure p around the projectile {see eqs. (14), (69), and (70) in Ref. [8])}.

$$F(x_e) = \frac{1}{2\pi} \cdot \int_0^{x_e} \frac{A''_{e,m}(t)}{\sqrt{x_e - t}} dt \tag{1}$$

$$\frac{p(x) - p_\infty}{p_\infty} \approx \frac{\gamma \cdot M^2}{(2 \cdot h \cdot \beta)^{\frac{1}{2}}} \cdot F(x_e) \text{ with } x = x_e + h \cdot \beta - \sqrt{h} \cdot \frac{(\gamma + 1) \cdot M^4}{\sqrt{2 \cdot \beta^3}} \cdot F(x_e) \tag{2}$$

Here M is the cruise Mach of the supersonic projectile, $\beta = \sqrt{M^2 - 1}$, the pressure distribution p is defined at a longitudinal line of h ft away from the projectile flying along the x-axis, and $A_{e,m}$ is the equivalent area of the supersonic configuration calculated using the Mach angle cut method {see sec. IV in Ref. [9] for the definition of $A_{e,m}$}.

In a review of Whitham's ingenious solution by Carlson and Maglieri [9], the following simplified approximation formula without nonlinear longitudinal correction was introduced {see p. 680 of Ref. [9]}.

$$\frac{p(x_e + h \cdot \beta) - p_\infty}{p_\infty} \approx \frac{\gamma \cdot M^2}{(2 \cdot h \cdot \beta)^{\frac{1}{2}}} \cdot \frac{1}{2\pi} \cdot \int_0^{x_e} \frac{A''_{e,m}(t)}{\sqrt{x_e - t}} dt \tag{3}$$

Equation (3) was used by Seebass and George {see eq. (6) in Ref. [10]} to study shapes of undertrack sonic boom ground signatures with minimum overpressure magnitude or minimum pressure rise through the shock wave. They derived the corresponding optimal F-functions for the shaped ground signatures and inverted Eq. (1) to obtain the equivalent area from the F-function.

$$A_{e,m}(x_e) = 4 \cdot \int_0^{x_e} F(t) \cdot \sqrt{x_e - t}\, dt \tag{4}$$

Equation (4) was only explicitly given by Seebass and George for $x_e = l_e$ {see eq. (7) in Ref. [10]}, but it holds for all $x_e \geq 0$. One can derive Eq. (4) from Eq. (1) using standard calculus methods. First, substitute $F(t)$ in Eq. (4) using Eq. (1) to get a double integral. Then change the order of integration for the double integral. Perform integration by substitution three times to get the analytical solution of the inner integral as a linear function multiplied by $A''_{e,m}$. Finally, use integration by parts to verify that the right hand side of Eq. (4) equals $A_{e,m}(x_e)$. This derivation of Eq. (4) uses the following properties of $A_{e,m}$: 1) $A'_{e,m}(x_e)$ is a continuous function, 2) $A'_{e,m}(0) = A_{e,m}(0) = 0$, and 3) $A''_{e,m}(x_e)$ exists except at a finite number of locations of x_e and $|A''_{e,m}(x_e)|$ is bounded by a constant. The value of $A_{e,m}(l_e)$ is completely determined by the cruise condition of the underlying supersonic configuration {see eq. (7) in Ref. [10]}.

$$A_{e,m}(l_e) = \frac{\beta}{\rho_\infty \cdot U_\infty^2} \cdot W_{crs} \tag{5}$$

In Eq. (5), W_{crs} is the cruise weight, ρ_∞ is the air density at the cruise altitude H, and U_∞ is the freestream velocity for cruise Mach M at H. Equation (5) leads to an inverse design optimization method for low-boom supersonic configurations: 1) choose a shaped ground signature form, 2) compute the corresponding optimal F-function for the cruise condition, and 3) shape a supersonic configuration so that its $A_{e,m}$ matches the equivalent area of the optimal F-

function. Darden extended the Seebass-George sonic boom minimization theory from an isothermal atmosphere to the real atmosphere [11].

Various extensions of F-function forms for sonic boom minimization were proposed for different ground signature shapes [12-15] or for inclusion of other design goals such as drag [16] and cruise trim [17]. The most advanced study [18] for inverse design of $A_{e,m}$ matches $A_{e,CFD}$ of a wing-body configuration with a low-boom $A_{e,m}$ target generated using the F-function form in Ref. [13]. Unfortunately, there is no theory that guarantees the accuracy of Eq. (3) for an arbitrary wing-body configuration.

The current state-of-the-art sonic boom analysis [19,20] uses CFD off-body pressure at an altitude location at least three body lengths (3BL) away from the aircraft and propagates the off-body pressure through the atmosphere using an augmented Burgers equation [21,22] to get the ground signature. For convenience, such a propagated undertrack ground signature will be called *CFD-based ground signature*. For a wing-body configuration, the ground signature propagated from $A_{e,CFD}$ might have a very different aft shape when compared to the CFD-based ground signature {see fig. 2 in Ref. [3]}. So, in general, Eq. (3) is not accurate for CFD off-body pressure at 3BL below a wing-body configuration. The Seebass-George-Darden sonic boom minimization theory is not applicable to design of low-boom supersonic aircraft when CFD off-body pressure at 3BL below the aircraft is used for sonic boom analysis. For convenience, design of low-boom supersonic aircraft using CFD undertrack off-body pressure for sonic boom analysis will be called *CFD-based low-boom design*.

The reversed equivalent area $A_{e,r}$ [3] can be considered as a correction of $A_{e,m}$ for an accurate BOR approximation of a supersonic aircraft. It is obtained by a composition of Eqs. (4), (1), and (3) with p replaced by p_r, which is computed using a reverse propagation of the undertrack pressure p at the off-body location of h ft (= 3BL) below the aircraft to the location of h_0 (= 50) ft below the aircraft.

$$A_{e,r}(x_e) = 4 \cdot \frac{(2 \cdot h_0 \cdot \beta)^{\frac{1}{2}}}{\gamma \cdot M^2} \cdot \int_0^{x_e} \left(\frac{p_r(t + x_0) - p_\infty}{p_\infty} \right) \cdot \sqrt{x_e - t}\, dt \tag{6}$$

The value of h_0 (= 50 ft) is selected to balance the accuracy of the linear approximation $x = x_e + h \cdot \beta$ for the nonlinear longitudinal location in Eq. (2) and the need to avoid excessive numerical errors of the reverse pressure propagation [3] near the supersonic aircraft using an augmented Burgers equation. The offset x_0 must be the initial pressure rise location of p_r. If x_0 were ahead of the initial pressure rise location of p_r, then $A_{e,r}(x_e) = 0$ for x_e up to the initial pressure rise location of p_r and $A_{e,r}$ could not be the equivalent area of a BOR with its pointed nose at $x_e = 0$. If x_0 were behind the initial pressure rise location of p_r, then $A_{e,r}$ would be unrelated to a nonzero segment of p_r and could not be used to recover p_r. In practice, due to numerical errors, it is difficult to identify the exact location of x_0. Fortunately, a low-boom supersonic aircraft usually has a long pointed front body and the front part of CFD off-body pressure below the aircraft is similar to the pressure converted from $A_{e,CFD}$ using Eq. (3). So, $A_{e,r}(x_e) \approx A_{e,CFD}(x_e)$ should hold for the front body portion of the aircraft. This leads to the following least squares fitting problem for automatic identification of x_0.

$$\min_{x_0} \int_0^{x_{frt}} \left(A_{e,r}(x_e) - A_{e,CFD}(x_e) \right)^2 dx_e \tag{7}$$

Here x_{frt} is the effective distance location of the leading edge of the root airfoil of the most forward lifting surface. Equation (7) for automatic identification of x_0 has not been published before and is very useful for calculating $A_{e,r}$.

One important property of $A_{e,r}$ is that $A_{e,r}(x_e) \approx A_{e,CFD}(x_e)$ does hold for the front body portion of any supersonic configuration with a long pointed front body, which has been confirmed numerically in all conducted $A_{e,r}$ analyses of such configurations. Moreover, it has been verified numerically that a low-boom supersonic aircraft and the corresponding $A_{e,r}$ have approximately the same CFD-based ground signature [3] {see also fig. 12b in Ref. [7]}. Now, a mathematical proof is provided to verify that the BOR defined by $A_{e,r}$ can be an accurate approximation of a low-boom supersonic aircraft for undertrack sonic boom analysis using CFD off-body pressure.

Let $\boldsymbol{B}_r$ be the BOR such that its $A_{e,m}$ equals $A_{e,r}$ of a low-boom supersonic aircraft. Then the F-function for $\boldsymbol{B}_r$, denoted by F_r, has the following form [see Eqs. (4) and (6)].

$$F_r(x_e) = \frac{(2 \cdot h_0 \cdot \beta)^{\frac{1}{2}}}{\gamma \cdot M^2} \cdot \frac{p_r(x_e + x_0) - p_\infty}{p_\infty} \tag{8}$$

Because Eq. (2) is accurate for a BOR with weak shocks, the following approximation holds for the pressure $p(x, \boldsymbol{B}_r)$ at h_0 ft below $\boldsymbol{B}_r$.

$$\frac{p(x,\boldsymbol{B}_r)-p_\infty}{p_\infty} \approx \frac{\gamma\cdot M^2}{(2\cdot h_0\cdot\beta)^{\frac{1}{2}}}\cdot F_r(x_e) \text{ with } x = x_e + h_0\cdot\beta - \sqrt{h_0}\cdot\frac{(\gamma+1)\cdot M^4}{\sqrt{2\cdot\beta^3}}\cdot F_r(x_e) \tag{9}$$

Comparing Eqs. (8) and (9), the nearfield pressure of $\boldsymbol{B}_r$ differs from p_r with a potential longitudinal location error of

$$x_0 - h_0\cdot\beta + \sqrt{h_0}\cdot\frac{(\gamma+1)\cdot M^4}{\sqrt{2\cdot\beta^3}}\cdot F_r(x_e) \tag{10}$$

First assume that the last term in Eq. (10) is negligible for sonic boom analysis of $\boldsymbol{B}_r$. Then we get $p(x_e+h_0\cdot\beta, \boldsymbol{B}_r) \approx p(x, \boldsymbol{B}_r)$. It follows from Eqs. (8) and (9) that $p(x_e+h_0\cdot\beta, \boldsymbol{B}_r) \approx p_r(x_e+x_0)$. The propagated waveform of $p(x_e+h_0\cdot\beta, \boldsymbol{B}_r)$ is approximately the same as that of $p_r(x_e+x_0)$ using the augmented Burgers equation for the propagation. At h ft below the aircraft, which is the initial altitude location for the reverse propagation to compute p_r, the propagated waveform of $p_r(x_e+x_0)$ approximately equals $p(x_e+x_0)$. So, the propagated waveform for $p(x, \boldsymbol{B}_r)$ approximately recovers the pressure $p(x_e+x_0)$ at h ft below the aircraft, which implies that the low-boom supersonic aircraft and its BOR approximation $\boldsymbol{B}_r$ have approximately the same CFD-based ground signature shape propagated from the off-body pressure $p(x_e)$ or $p(x_e+x_0)$.

In theory, when h_0 is close to 0, the last term in Eq. (10) is negligible, which justifies why h_0 should be as small as possible to define $A_{e,r}$. The choice of h_0 = 50 ft is based on the empirical data about the numerical accuracy of the reverse propagation solver [3] to compute p_r. Due to excessive numerical errors from the reverse propagation solver near the aircraft, the propagation of the computed p_r for $h_0 < 50$ ft from the altitude ($H–h_0$) to the altitude at 3BL below the aircraft might yield a pressure distribution that is significantly different from the original $p(x)$ at 3BL below the aircraft. In contrast, for h_0 = 50 ft, the propagated waveform of p_r from the altitude ($H–h_0$) to the altitude at 3BL below the aircraft is always nearly identical to the original $p(x)$ at 3BL below the aircraft. In general, the accuracy of Eq. (3) [i.e., Eq. (2) without nonlinear longitudinal correction] for p around a pointed BOR with weak shocks needs further study. Also, it will be valuable to generate $\boldsymbol{B}_r$ using inverse design optimization and directly compare the undertrack ground signatures of $\boldsymbol{B}_r$ and the supersonic configuration. But the optimization problem for $\boldsymbol{B}_r$ is nontrivial.

Because the undertrack ground signatures propagated from $A_{e,r}$ and the off-body pressure at 3BL below the aircraft have approximately the same PLdB value and shape {e.g., see fig. 12b in Ref. [7]}, shaping an aircraft for a low-boom $A_{e,r}$ shape is numerically equivalent to shaping the aircraft for a low-boom off-body pressure at 3BL below the aircraft. That is, $A_{e,r}$ and the off-body pressure at 3BL below the aircraft have approximately the same undertrack ground signature. This proves that $A_{e,r}$ represents an accurate BOR approximation of the supersonic aircraft for undertrack sonic boom analysis.

The choice of h_0 = 3BL can avoid the reverse pressure propagation to define an equivalent area by Eq. (6) with $p_r(x)$ replaced by $p(x)$, followed by converting the equivalent area back to $p(x)$ using Eq. (3) with h = 3BL. Then, it seems that the off-body pressure at 3BL below the aircraft and the equivalent area defined without reverse pressure propagation have the same undertrack ground signature. However, this approach ignores the potentially significant approximation errors in Eq. (3) due to removal of the nonlinear longitudinal correction term in Eq. (2). The supersonic configuration and the BOR corresponding to this equivalent area could have significantly different undertrack ground signatures.

The definition of $A_{e,r}$ using $p(x)$ at 3BL below the aircraft was based on extensive numerical results, which confirmed that, for any given supersonic configuration, the undertrack ground signature for $p(x)$ at h ft below the configuration was approximately invariant with respect to h if $h \geq$ 3BL. In other words, after 3BL, the three-dimensional downward propagation of $p(x)$ using the Euler equation is almost equivalent to the two-dimensional downward propagation of $p(x)$ using the augmented Burgers equation. It is also pointed out in Ref. [19] that $p(x)$ at 3BL below the aircraft is an acceptable choice for undertrack sonic boom analysis, based on the previous case studies for the First and Second AIAA Sonic Boom Prediction Workshops. See the first paragraph of the right column after fig. 6 in Ref. [19].

The most useful property of $A_{e,r}$ is that $A_{e,r}(\boldsymbol{D}) \approx A_{e,r}(\boldsymbol{D}_0) + A_{e,CFD}(\boldsymbol{D}) - A_{e,CFD}(\boldsymbol{D}_0)$ holds [23] for a baseline configuration $\boldsymbol{D}_0$ and another supersonic configuration $\boldsymbol{D}$ if h_0 = 50 ft and the differences between outer mold lines of $\boldsymbol{D}$ and $\boldsymbol{D}_0$ are small. This approximation formula enables an accurate prediction of $A_{e,r}$ for a newly generated design $\boldsymbol{D}$ in optimization iteration using the CFD surface solution of $\boldsymbol{D}$ and the existing off-body solution of $\boldsymbol{D}_0$. The accurate

approximation of $A_{e,r}(\boldsymbol{D})$ using $A_{e,CFD}(\boldsymbol{D})$ is critical for the successful simultaneous optimization of a low-boom inverse design objective and a mission performance objective using the BCO method [7]. The choice of h_0 has a significant effect on the accuracy of this approximation formula. A larger value of h_0 means potentially larger misalignments of the corresponding shock locations for the pressure on the aircraft surface and $p_r(x)$ {see fig. 3 in Ref. [6]}, which could invalidate the approximation formula for $A_{e,r}(\boldsymbol{D})$.

Different from $A_{e,m}(l_e)$, the value of $A_{e,r}(l_e)$ is not directly related to the cruise weight of the corresponding supersonic aircraft. A ratio parameter μ can be used to denote $A_{e,r}(l_e)/A_{e,CFD}(l_e)$, which relates $A_{e,r}(l_e)$ to W_{crs}.

$$A_{e,r}(l_e) = \mu \cdot A_{e,CFD}(l_e) = \mu \cdot \frac{\beta}{\rho_\infty \cdot U_\infty^2} \cdot W_{crs} \tag{11}$$

The BOR corresponding to $A_{e,r}$ captures all the three-dimensional effects of the supersonic configuration for the undertrack sonic boom analysis. All the available numerical results indicate that $A_{e,r}(l_e) > A_{e,CFD}(l_e)$. But there is no theoretical interpretation for the value of $A_{e,r}(l_e)$. Equation (11) was based on the empirical observation when conducting the low-boom MDO studies in Refs. [7,24], which indicate that $A_{e,r}(l_e)/A_{e,CFD}(l_e)$ of an existing low-boom configuration provides an accurate prediction of $A_{e,r}(l_e)/A_{e,CFD}(l_e)$ of another low-boom configuration if the two low-boom configurations have similar component topologies. Here the component topology means how the aircraft components are connected. For low-boom supersonic transports with two engines installed on the sides of the fuselage [7,24], the available data indicates that μ is between 1.21 and 1.25. It is worth pointing out that the expected approximate invariance of μ only needs to be true for low-boom supersonic configurations with similar component topologies. A significant difference of two μ values for two arbitrary supersonic configurations does not hinder the application of Eq. (11) for coupling the low-boom inverse design optimization and mission performance optimization.

Another important parameter for $A_{e,r}$ is $A_{e,r}(l_e/2)/A_{e,r}(l_e)$, which is called the trim ratio [7,24]. This ratio is implicitly related to whether a low-boom supersonic aircraft satisfies the cruise trim constraint (i.e., the aircraft can maintain the designed low-boom shape for cruise flight using fuel redistributions for trim). It is well known that a low-boom supersonic aircraft tends to have the longitudinal CP too aft than the desired. For supersonic cruise efficiency, the fuselage and wing should be as small as possible while satisfying all the design requirements. For low-boom requirements, the aircraft should be as long as possible. There is not much flexibility for the longitudinal volume distribution once the component topology and the aircraft length are determined. So, the longitudinal CG is mainly determined by the fuel distribution. When the most aft longitudinal CG is still ahead of the longitudinal CP, one has to move the longitudinal CP forward. One standard option is to use control surface deflections for trim, but this will lead to an outer mold line different from the designed low-boom shape and might cause a significant increase of sonic boom ground noise level. Another option is to redesign the low-boom supersonic aircraft so that its longitudinal CP is ahead of the most aft longitudinal CG. This can be accomplished by enforcing $A_{e,r}(l_e/2)/A_{e,r}(l_e)$ to be large enough. For two low-boom supersonic aircraft with similar component topologies, a larger value of $A_{e,r}(l_e/2)/A_{e,r}(l_e)$ usually means a more forward location of the longitudinal CP. This leads to a trim ratio constraint for any $A_{e,r}$ target, say $A_{e,r}^{opt}$: $A_{e,r}^{opt}(l_e/2)/A_{e,r}^{opt}(l_e) \geq \delta$. This trim ratio constraint implies that $A_{e,r}(l_e/2)/A_{e,r}(l_e)$ of the optimal solution of the inverse design optimization using $A_{e,r}^{opt}$ as the target is approximately bounded below by δ because $A_{e,r}(x_e) \approx A_{e,r}^{opt}(x_e)$. So, δ should be as large as possible for the inverse design optimization solution to satisfy the cruise trim constraint. However, as shown in the next section, a larger value of the trim ratio of an $A_{e,r}$ target means a higher PLdB value of its undertrack ground signature. So, the value of δ should be as small as possible for the inverse design optimization solution to attain the lowest sonic boom ground noise level. The trim ratio constraint for $A_{e,r}$ targets allows a compatible combination of the cruise trim and low-boom requirements before the inverse design optimization of $A_{e,r}$. If an $A_{e,r}$ target is determined without considering the cruise trim requirement, then any acceptable inverse design solution for the specified $A_{e,r}$ target might not be able to satisfy the cruise trim constraint because the acceptable inverse design solution might require a longitudinal lift distribution that is not compatible with the cruise trim constraint. The best compromise between the cruise trim and low-boom requirements is difficult to determine a priori. A trial-and-error method was used to determine an appropriate value of δ [7,24].

With Eq. (11) and a lower bound δ to control the trim ratio, an inverse design optimization method can be used for development of low-boom supersonic aircraft: 1) find an $A_{e,r}$ target denoted by $A_{e,r}^{opt}$ such that $A_{e,r}^{opt}(l_e) = (\mu \cdot \beta \cdot W_{crs})/(\rho_\infty \cdot U_\infty^2)$ and $A_{e,r}^{opt}(l_e/2)/A_{e,r}^{opt}(l_e) \geq \delta$, and 2) shape the supersonic configuration such that its $A_{e,r}$ matches $A_{e,r}^{opt}$. There are different choices for an $A_{e,r}$ target. For example, one could choose an $A_{e,r}$ target that has the minimum magnitude for undertrack ground signature. However, based on the NASA N+3 low-boom goal [25,26] for an acceptable sonic boom ground noise level below 70 PLdB, the PLdB value of the undertrack ground signature for an

$A_{e,r}$ target will be used as the objective for optimization of the $A_{e,r}$ target. This ensures that the optimized $A_{e,r}$ target for inverse design optimization has the lowest PLdB among all possible $A_{e,r}$ targets.

III. Equivalent Area Targets for Different Low-Boom Cruise Conditions

This section includes numerical examples to verify that, for different cruise conditions and $A_{e,r}$ targets defined by Bezier curves with eight control points, all $A_{e,r}$ targets optimized for PLdB can be approximately generated by scaling one of them under some constraints. To define an $A_{e,r}$ target, all design-related properties of the $A_{e,r}$ target are parameterized by the low-boom cruise condition $\boldsymbol{C} = (M, H, W_{crs})$, effective length l_e, and two nondimensional parameters δ and μ related to the midpoint and endpoint of the target. As discussed in the previous section, μ is an a priori estimate of $A_{e,r}(l_e)/A_{e,CFD}(l_e)$ and δ approximately determines the trim ratio $A_{e,r}(l_e/2)/A_{e,r}(l_e)$, for an expected inverse design solution. The methods for choosing δ and μ are discussed in the detailed explanation of fig. 7 in Ref. [7]. The following $A_{e,r}$ target optimization problem [7,24] minimizes PLdB of an $A_{e,r}$ target with two constraints defined using the given design-related parameters.

$$\min_{\boldsymbol{d}_{tgt}} \text{PLdB}(A_e) \text{ subject to } \frac{A_e\left(\frac{l_e}{2}\right)}{A_e(l_e)} \geq \delta \text{ and } A_e(l_e) = \frac{\mu \cdot \beta \cdot W_{crs}}{\rho_\infty \cdot U_\infty^2} \tag{12}$$

The equivalent area A_e in Eq. (12) is defined using a Bezier curve with eight control points $\{(x_{c,i}, y_{c,i}): 0 \leq i \leq 7\}$ (see Fig. 1). The following explicit formula is used to define the Bezier curve $(x(t), A_e(x(t)))$ for $0 \leq t \leq 1$. The first and last control points of the Bezier curve define the start point and endpoint of A_e, i.e., $x_{c,0} = y_{c,0} = 0$, $x_{c,7} = l_e$, and $y_{c,7} = A_e(l_e)$. The 12 coordinates of the remaining 6 control points are used as components of design vector $\boldsymbol{d}_{tgt}$ in Eq. (12). The Bezier curve in Fig. 1 is generated using $x_{c,0} = y_{c,0} = 0$, $x_{c,1} = 59.26$, $y_{c,1} = 1.082$, $x_{c,2} = 139.7$, $y_{c,2} = 8.503$, $x_{c,3} = 152.8$, $y_{c,3} = 247.1$, $x_{c,4} = 171.2$, $y_{c,4} = 175.9$, $x_{c,5} = 187.8$, $y_{c,5} = 221.1$, $x_{c,6} = 197.3$, $y_{c,6} = 224.8$, $x_{c,7} = 250$, and $y_{c,7} = 225$.

$$x(t) = \sum_{i=0}^{7} x_{c,i} \cdot \frac{7!}{i!\,(7-i)!} \cdot t^i \cdot (1-t)^{7-i}$$

$$A_e\big(x(t)\big) = \sum_{i=0}^{7} y_{c,i} \cdot \frac{7!}{i!\,(7-i)!} \cdot t^i \cdot (1-t)^{7-i} \qquad \text{for } 0 \leq t \leq 1$$

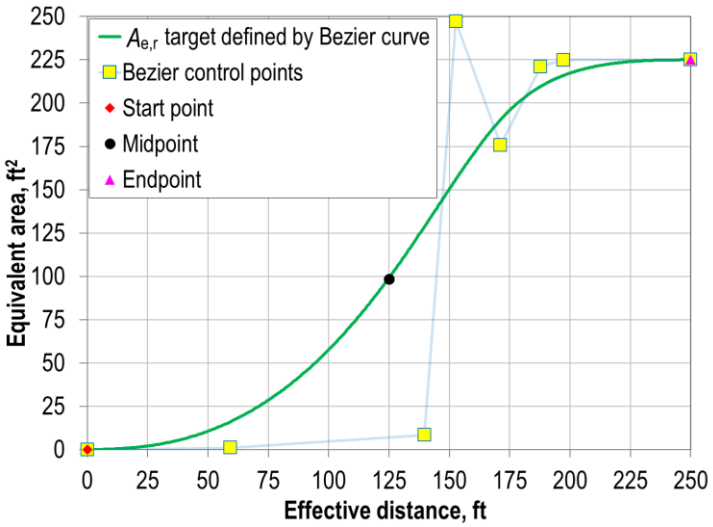

Fig. 1 Bezier curve with eight control points to define A_e.

In theory, any $A_{e,r}$ target must satisfy three important properties of $A_{e,m}$: 1) $A'_{e,m}(x_e)$ is a continuous function, 2) $A'_{e,m}(0) = 0$, and 3) $A'_{e,m}(l_e) = 0$. The first property is required for Eq. (1). The second property can be derived mathematically from Eq. (4) and $F(0) = 0$. But an intuitive argument is included here. A low-boom supersonic aircraft

usually has a fuselage with a pointed nose. The maximum diameter of a fuselage cross section is less than a constant multiple of the distance from the cross section to the fuselage nose. The lift distribution near the fuselage nose is almost zero. So, $A_{e,m}(x_e)$ is bounded by a constant multiple of x_e^2 for x_e near zero, which implies $A'_{e,m}(0) = 0$. The third property follows the definition of $A_{e,m}$. Because the equivalent area due to volume is zero for $x_e > l_e$ and the equivalent area due to lift is a constant for $x_e > l_e$, $A_{e,m}(x_e) = A_{e,m}(l_e)$ for $x_e \geq l_e$, which implies $A'_{e,m}(l_e) = 0$. Any Bezier curve that defines an $A_{e,r}$ target has a continuous derivative for $0 \leq x_e \leq l_e$. The other two required properties of $A_{e,m}$ could be enforced by using $y_{c,1} = 0$ and $y_{c,6} = y_{c,7}$. The condition $A'_e(l_e) = 0$ allows $A_e(x_e)$ defined for $0 \leq x_e \leq l_e$ to be extended using $A_e(x_e) = A_e(l_e)$ for $x_e > l_e$ and ensures the continuity of $A'_e(x_e)$ at $x_e = l_e$ for the extended $A_e(x_e)$. The constraints $A'_e(0) = 0$ and $A'_e(l_e) = 0$ reduce the degree of freedom by 2 for the Bezier curve and are not explicitly enforced for $A_e(x_e)$ in Eq. (12). The main reason is that the optimal solution of Eq. (12) usually has nearly horizontal tangent lines at $x_e = 0$ and $x_e = l_e$ (see Fig. 1). Another reason is that a discrete approximation of $A''_e(x_e)$ is used to compute the near-field pressure distribution $p(x)$ using Eq. (3) with $A''_{e,m}$ replaced by A''_e. The exact values of $A'_e(0)$ and $A'_e(l_e)$ are not used in the calculation of $p(x)$. However, if $A'_e(0) \approx 0$ or $A'_e(l_e) \approx 0$ is violated, then $A_e(x_e)$ cannot be used as an $A_{e,r}$ target for inverse design optimization of $A_{e,r}$.

For any $A_e(x_e)$ defined by a Bezier curve, a discrete form of $A_e(x_e)$ is computed using 501 equally spaced values of t between 0 and 1. The corresponding nearfield undertrack pressure p at altitude of $(H–h_0)$ is defined by Eq. (3) with $h = h_0$ and $A_{e,m}$ replaced by A_e. Because $p(x_e+h\cdot\beta)$ is usually nonzero for $x_e > l_e$ and must be defined using Eq. (3), the domain of $A_e(x_e)$ is expanded using $A_e(x_e) = A_e(l_e)$ for $x_e > l_e$ to mimic $A_{e,m}(x_e)$. Fifty equally spaced points from $x_e = l_e$ to $x_e = 1.5\cdot l_e$ (not including $x_e = l_e$) are used to generate fifty points of $A_e(x_e)$ after $x_e = l_e$. The computed values of $A_e(x_e)$ are used to obtain the approximate values of $A''_e(x_e)$ at the 551 locations of x_e. The integral in Eq. (3) can be evaluated exactly to compute p if $A''_{e,m}(x_e)$ is replaced by the piecewise linear approximation of $A''_e(x_e)$ using the generated 551 data points for $A''_e(x_e)$. The solver for an augmented Burgers equation [22] is used to compute the undertrack ground signature for A_e by propagating p through the standard atmosphere [27] from the altitude $(H–h_0)$ to the ground (at altitude of 0 ft). The humidity profile for the standard atmosphere is based on ANSI S1.26 [28]. The method in Ref. [1] is used to compute PLdB of the ground signature, denoted by PLdB(A_e). The optimal solution of Eq. (12) is denoted by $A_{e,r}^{opt}$**.** A derivative-free optimization solver, the Design Explorer in ModelCenter [29], is used to compute $A_{e,r}^{opt}$. The termination condition for the Design Explorer ensures that $A_{e,r}^{opt}$ is at least a local optimum. Equation (12) might have multiple local minimums. Multiple solutions of Eq. (12) with different initial guesses should be computed to empirically ensure that the generated optimal solution is the best one. Obviously, $A_{e,r}^{opt}$ varies with the cruise condition $\boldsymbol{C}$ and effective length l_e. However, the following nondimensional form $A_{e,r,0}^{opt}$ of $A_{e,r}^{opt}$ is approximately invariant with respect to changes of $\boldsymbol{C}$ when μ, δ, and l_e are fixed.

$$A_{e,r,0}^{opt}(t) = \frac{\rho_\infty \cdot U_\infty^2}{\mu \cdot \beta \cdot W_{crs}} \cdot A_{e,r}^{opt}(t \cdot l_e) \text{ for } 0 \leq t \leq 1 \tag{13}$$

Invariance of nondimensional form of $A_{e,r}^{opt}$. *Let* $l_e > 0$, $\mu \geq 1$, *and* $0 \leq \delta < 1$ *be fixed. Then the nondimensional* $A_{e,r}$ *target* $A_{e,r,0}^{opt}$ *in Eq.* (13) *is approximately invariant with respect to changes of* $\boldsymbol{C}$ *if* $\text{PLdB}(A_{e,r}^{opt}) \leq 70$. *That is, for any two vectors* $\boldsymbol{C}_1$ *and* $\boldsymbol{C}_2$, *if* $\text{PLdB}(A_{e,r}^{opt}(\boldsymbol{C}_1, l_e)) \leq 70$ *and* $\text{PLdB}(A_{e,r}^{opt}(\boldsymbol{C}_2, l_e)) \leq 70$, *then*

$$A_{e,r,0}^{opt}(t, \boldsymbol{C}_1, l_e) \approx A_{e,r,0}^{opt}(t, \boldsymbol{C}_2, l_e) \qquad \text{for } 0 \leq t \leq 1 \tag{14}$$

At the moment, no mathematical proof of Eq. (14) is available. Equation (14) will only be verified numerically with minor differences between $A_{e,r,0}^{opt}(t, \boldsymbol{C}_1, l_e)$ and $A_{e,r,0}^{opt}(t, \boldsymbol{C}_2, l_e)$, which means the approximate invariance of $A_{e,r,0}^{opt}$ with respect to changes of $\boldsymbol{C}$ because of the approximation errors in Eq. (14).

The constraint $\text{PLdB}(A_{e,r}^{opt}) \leq 70$ is only used for $A_{e,r}$ targets that satisfy the NASA N+3 low-boom goal [25,26] and Eq. (14) might also hold for targets with higher PLdB values. Moreover, Eq. (14) holds for different μ values. In fact, because $A_{e,r}^{opt}$ only depends on $\mu\cdot W_{crs}$, a change of μ is equivalent to a change of W_{crs} with the same resulting $\mu\cdot W_{crs}$. The assumption of a fixed l_e for Eq. (14) can be relaxed. In fact, the validity of Eq. (14) for a minor difference of l_e values between the two targets in Eq. (14) will also be confirmed by the following numerical examples. For practical applications of Eq. (14) in low-boom MDO, it suffices to verify that Eq. (14) holds in a much limited setting. The invariance with respect to changes of M is not required for application of Eq. (14) in low-boom MDO [7]. So, M can be fixed unless M is a design objective in low-boom MDO [24]. The tested values of M for Eq. (14) are 1.7 and 1.8, but Eq. (14) is expected to be true for $1.4 \leq M \leq 2$. Equation (14) is usually an equality if only H changes between 45

kft and 60 kft. Equation (14) is also expected to be true for the l_e value of any given low-boom supersonic aircraft (from 100 ft for a demonstrator to 250 ft for a transport). The allowable range of l_e for Eq. (14) is determined by small variations of l_e due to changes of angle of attack of the supersonic configuration used for low-boom MDO. Because PLdB($A_{e,r}^{opt}$) is an increasing function of W_{crs}, the upper bound of W_{crs} is implicitly determined by the upper limit of PLdB($A_{e,r}^{opt}$), which is 70 PLdB in this paper. The maximum value of PLdB($A_{e,r}^{opt}$) for the validity of Eq. (14) has not been established due to the focus on the NASA N+3 low-boom goal in this paper. It will also be interesting to check whether Eq. (14) is still valid if other parametric curves (such as Bezier curves with nine control points or B-splines) are used to define $A_{e,r}$ targets.

For numerical verification of Eq. (14), the parameter μ is fixed at 1.23, which is the mid value of the observed range from 1.21 to 1.25 for $A_{e,r}(l_e)/A_{e,CFD}(l_e)$ of the generated low-boom configurations [7,24]. The exact value of μ is not important because Eqs. (12) and (13) show that $A_{e,r}^{opt}$ only depends on $\mu \cdot W_{crs}$. Any variation of μ is implicitly included in the variation of W_{crs}. For convenience, the change of W_{crs} is implicitly represented by the change of $A_e(l_e)$, which depends on μ, W_{crs}, M, and H [see Eq. (12)]. Two values of δ at 0 and 0.448 are selected to verify Eq. (14). These two values were used to generate $A_{e,r}$ targets for low-boom MDO studies in Refs. [7,24].

For $\delta = 0$, l_e is fixed at 250 ft. Eight different cases of $\{A_e(l_e), M, H\}$ are used to verify Eq. (14). For these cases, W_{crs} changes with $\{A_e(l_e), M, H\}$ using the equality constraint in Eq. (12). The $A_{e,r,0}^{opt}$ shapes are compared in Fig. 2. The mean curve is the average of the eight nondimensional $A_{e,r}$ targets. The min and max absolute difference curve show the minimum and maximum absolute differences between any two curves, respectively. The nonzero values of the min absolute difference curve show that all nondimensional $A_{e,r}$ targets are different. The maximum absolute differences between any two target curves are less than 0.006. Even though there is no trim ratio requirement for $A_{e,r}^{opt}$ [i.e., the midpoint constraint in Eq. (12) for $\delta = 0$ is always satisfied by any A_e], all generated targets have approximately the same trim ratio of 0.394.

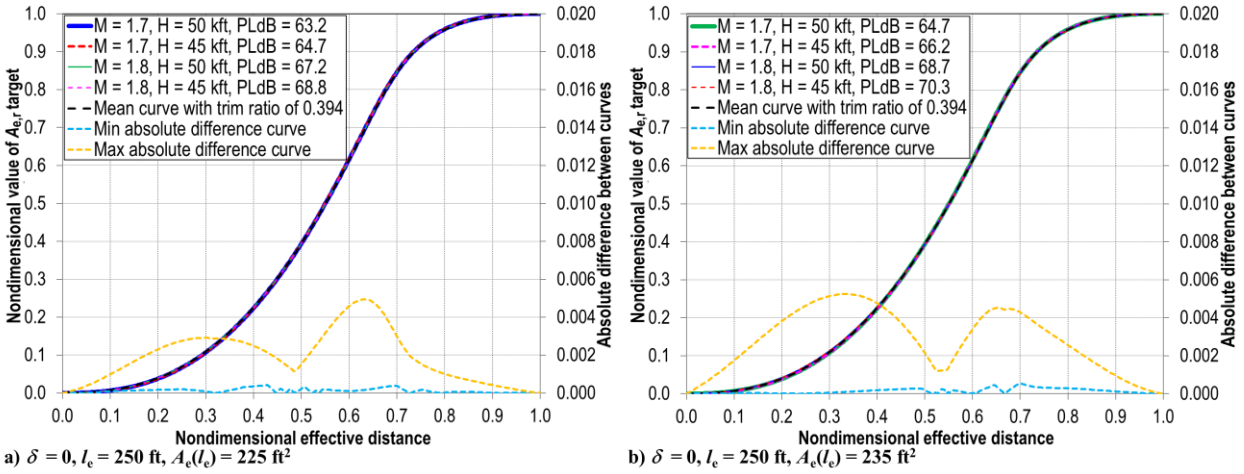

Fig. 2 Nondimensional forms of $A_{e,r}^{opt}$ for $\delta = 0$.

For $\delta = 0.448$, four different cases of $\{M, H\}$ are used to verify Eq. (14) for $l_e = 250$ ft and $A_e(l_e) = 225$ ft^2. Again, W_{crs} changes with $\{A_e(l_e), M, H\}$ using the equality constraint in Eq. (12). Figure 3a shows that Eq. (14) holds with the maximum absolute difference about 0.006. During the numerical verification of Eq. (14) for $l_e = 240$ ft, $A_{e,r,0}^{opt}$ is also approximately invariant with respect to changes of l_e. So, four different cases of $\{l_e, A_e(l_e)\}$ are used to verify Eq. (14) for $M = 1.7$ and $H = 55$ kft. The corresponding $A_{e,r,0}^{opt}$ shapes are compared in Fig. 3b. In this case, the maximum absolute difference between the $A_{e,r,0}^{opt}$ curves is slightly higher at 0.011, which is still negligible when compared to potential $A_{e,r}$ matching errors [7,24] from CFD-based low-boom inverse design optimization. The reference curve for trim ratio of 0.394 is included in Fig. 3 to show how the trim ratio constraint changes the $A_{e,r,0}^{opt}$ shapes, but it is not used in calculation of differences between the $A_{e,r,0}^{opt}$ curves. In general, for the same ($\boldsymbol{C}$, l_e, μ), PLdB($A_{e,r}^{opt}$) is an increasing function of the trim ratio $A_{e,r}^{opt}(l_e/2)/A_{e,r}^{opt}(l_e)$. The PLdB penalty for trim ratio increase can be determined by comparing the data from Figs. 2a and 3a for $H = 50$ ft. For example, if $M = 1.7$, $H = 50$ kft, $l_e = 250$ ft, and $A_e(l_e) = 225$ ft^2, then the PLdB of $A_{e,r}^{opt}$ increases from 63.2 to 65.7 when the trim ratio is raised from 0.394 to 0.448.

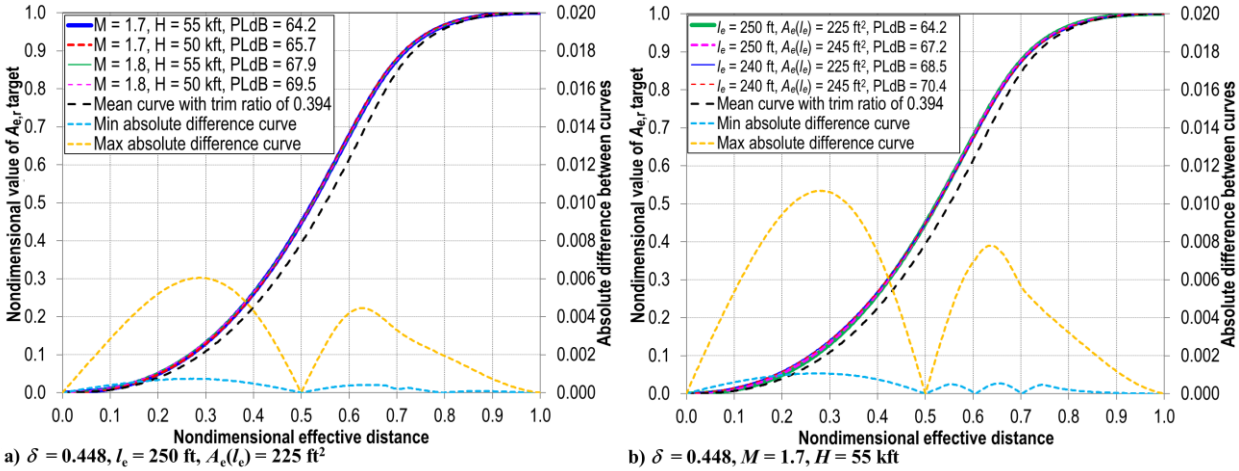

a) δ = 0.448, l_e = 250 ft, $A_e(l_e)$ = 225 ft² b) δ = 0.448, M = 1.7, H = 55 kft

Fig. 3 Nondimensional forms of $A_{e,r}^{opt}$ for δ = 0.448.

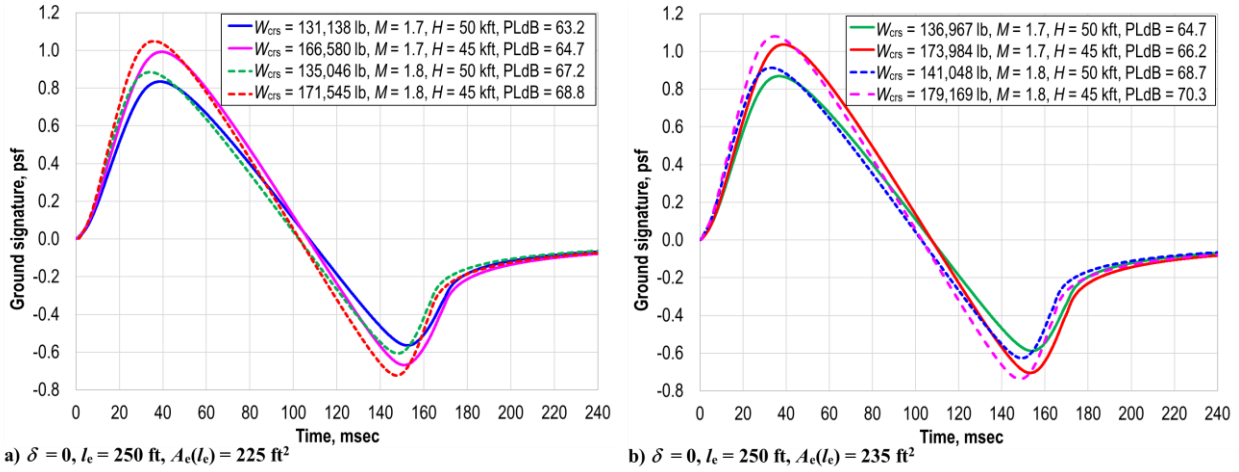

a) δ = 0, l_e = 250 ft, $A_e(l_e)$ = 225 ft² b) δ = 0, l_e = 250 ft, $A_e(l_e)$ = 235 ft²

Fig. 4 Undertrack ground signatures for $A_{e,r}^{opt}$ when δ = 0.

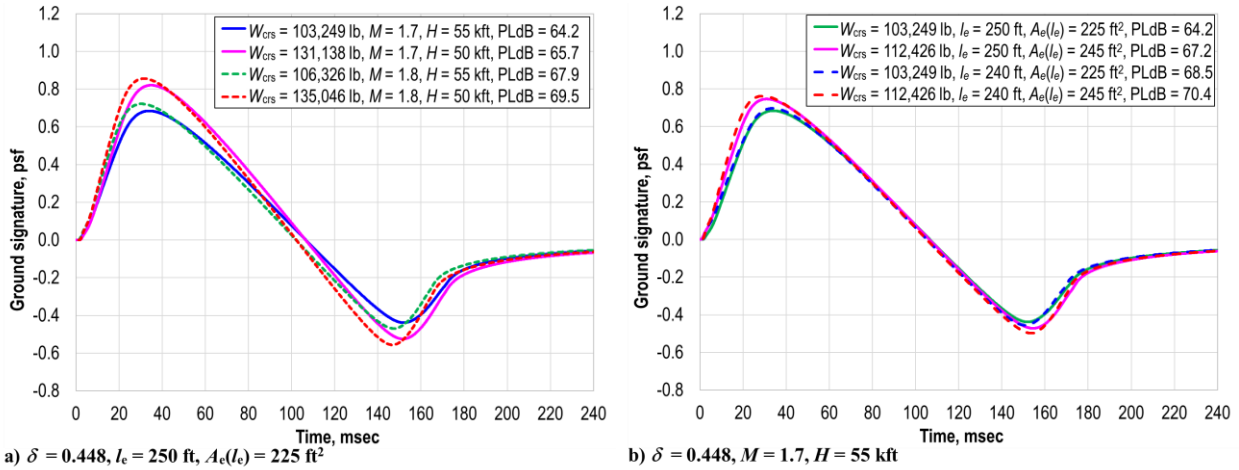

a) δ = 0.448, l_e = 250 ft, $A_e(l_e)$ = 225 ft² b) δ = 0.448, M = 1.7, H = 55 kft

Fig. 5 Undertrack ground signatures for $A_{e,r}^{opt}$ when δ = 0.448.

The ground signatures for all the $A_{e,r}$ targets in Figs. 2 and 3 are included in Figs. 4 and 5, respectively. It is counter intuitive that the optimal signatures for δ = 0 have much higher magnitudes than those for δ = 0.448 with similar PLdB values. However, the detrimental effects of higher signature magnitudes on PLdB are mitigated by the lower initial

signature rise slopes of the optimal signatures for $\delta = 0$ than those for $\delta = 0.448$. The corresponding targets for off-body pressures at three effective lengths below the aircraft are plotted in Figs. 6 and 7. These optimal *dp/p* targets have similar shapes. The optimal *dp/p* targets for $\delta = 0.448$ have stronger initial shocks and arise to the maximum magnitudes faster than those for $\delta = 0$.

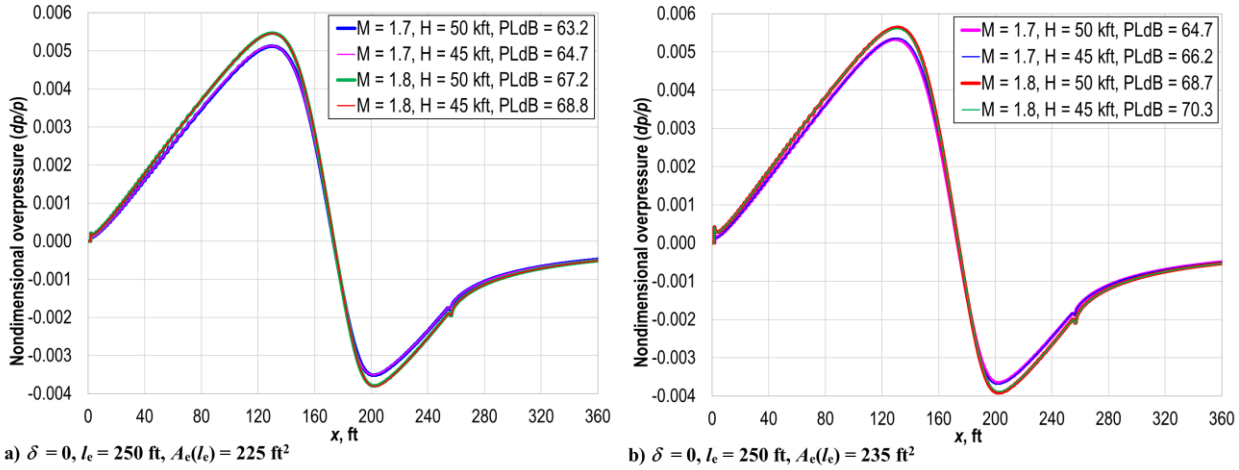

a) $\delta = 0$, $l_e = 250$ ft, $A_e(l_e) = 225$ ft^2 b) $\delta = 0$, $l_e = 250$ ft, $A_e(l_e) = 235$ ft^2

Fig. 6 Nondimensional overpressures of $A_{e,r}^{opt}$ at three effective lengths below cruise altitudes when $\delta = 0$.

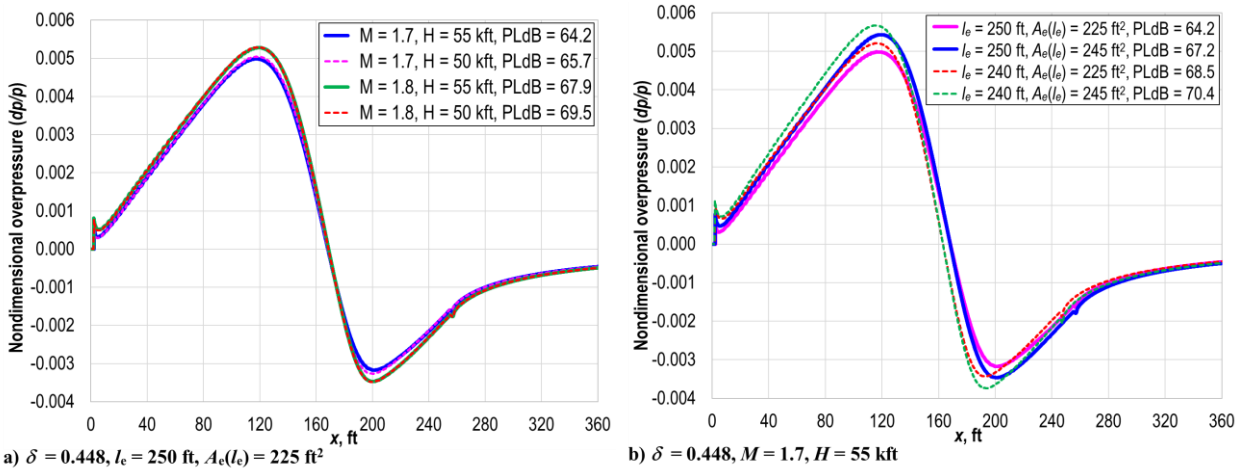

a) $\delta = 0.448$, $l_e = 250$ ft, $A_e(l_e) = 225$ ft^2 b) $\delta = 0.448$, $M = 1.7$, $H = 55$ kft

Fig. 7 Nondimensional overpressures of $A_{e,r}^{opt}$ at three effective lengths below cruise altitudes when $\delta = 0.448$.

An important application of Eq. (14) is the approximate optimality of the scaled $A_{e,r}$ targets generated using one optimized $A_{e,r}$ target for the design-related parameters of a baseline configuration. Consider the optimal solution $A_{e,r}^{opt}(\boldsymbol{C}_0, l_{e,0})$ of Eq. (12) for a given cruise condition $\boldsymbol{C}_0$ of a baseline configuration with an effective length $l_{e,0}$. For any cruise condition vector $\boldsymbol{C}$ and any effective length l_e, define the following scaled $A_{e,r}$ target.

$$A_{e,r}^{target}(x_e, \boldsymbol{C}, l_e) = \frac{A_{e,m}(l_e, \boldsymbol{C})}{A_{e,m}(l_{e,0}, \boldsymbol{C_0})} \cdot A_{e,r}^{opt}\left(\frac{l_{e,0}}{l_e} x_e, \boldsymbol{C}_0, l_{e,0}\right) \tag{15}$$

The value of $A_{e,m}(l_e, \boldsymbol{C})$ is determined by the cruise condition $\boldsymbol{C}$ and defined by Eq. (5). Equation (15) is an equivalent form of the target scaling formula [eq. (9)] in Ref. [7].

Optimality of scaled $A_{e,r}$ targets. *Let* $\mu \geq 1$ *and* $0 \leq \delta < 1$ *be fixed. If* $\text{PLdB}(A_{e,r}^{opt}(\boldsymbol{C}_0, l_{e,0})) \leq 70$, *then*

$$A_{e,r}^{target}(x_e, \boldsymbol{C}, l_e) \approx A_{e,r}^{opt}(x_e, \boldsymbol{C}, l_e) \text{ for } 0 \leq x_e \leq l_e \text{ whenever } \text{PLdB}(A_{e,r}^{opt}(\boldsymbol{C}, l_e)) \leq 70 \text{ and } l_e \approx l_{e,0} \tag{16}$$

If $l_e = l_{e,0}$, it follows from Eqs. (5), (13), and (15) that Eq. (16) is exactly Eq. (14) with $\boldsymbol{C}_1 = \boldsymbol{C}_0$ and $\boldsymbol{C}_2 = \boldsymbol{C}$. Figure 3b shows that Eq. (16) holds for $\delta = 0.448$ and a difference of 10 ft for $|l_e - l_{e,0}|$. To give an intuitive perspective of what Eq. (16) means, two optimized $A_{e,r}$ targets are generated by solving Eq. (12) for $(\boldsymbol{C}_1, l_{e,1})$ and $(\boldsymbol{C}_2, l_{e,2})$ listed on the top of Fig. 8a. The values of μ and δ are fixed at 1.22 and 0.448, respectively. Let $A_{e,r}^{target}(\boldsymbol{C}_1, l_{e,1})$ and $A_{e,r}^{target}(\boldsymbol{C}_2, l_{e,2})$ be scaled from $A_{e,r}^{opt}(\boldsymbol{C}_2, l_{e,2})$ and $A_{e,r}^{opt}(\boldsymbol{C}_1, l_{e,1})$, respectively, using Eq. (15). Figure 8a shows that $A_{e,r}^{opt}(\boldsymbol{C}_1, l_{e,1}) \approx A_{e,r}^{target}(\boldsymbol{C}_1, l_{e,1})$ and $A_{e,r}^{opt}(\boldsymbol{C}_2, l_{e,2}) \approx A_{e,r}^{target}(\boldsymbol{C}_2, l_{e,2})$. That is, each optimized $A_{e,r}$ target can be approximately obtained by scaling the other optimized $A_{e,r}$ target using Eq. (15). The undertrack ground signature for $A_{e,r}^{target}(\boldsymbol{C}_1, l_{e,1})$ has a lower maximum magnitude than that for $A_{e,r}^{opt}(\boldsymbol{C}_1, l_{e,1})$, while the former has a higher initial signature rise slope and a slightly higher PLdB value than the latter (see Fig. 8b, where the signatures corresponding to the cruise condition $\boldsymbol{C}_1$ are shifted to the right for a clear view of the initial signature rise slopes).

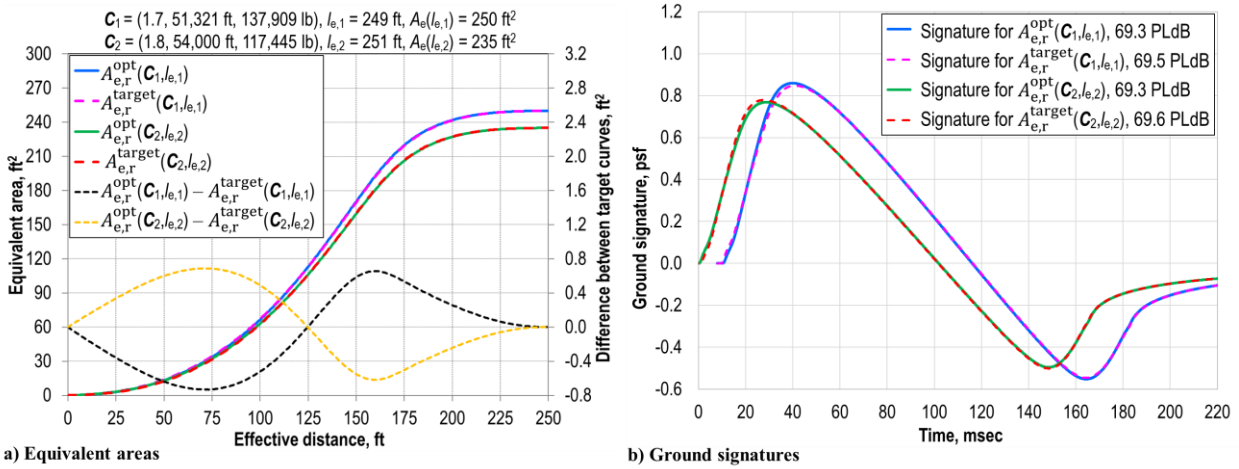

Fig. 8 Approximate optimality of the scaled $A_{e,r}$ targets.

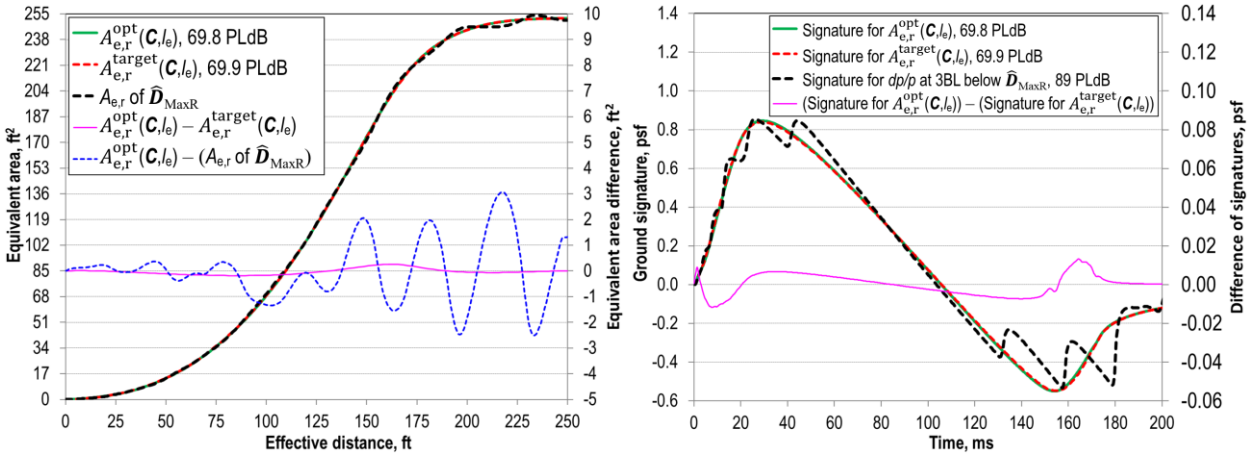

Fig. 9 $A_{e,r}$ targets and their undertrack ground signatures for low-boom design.

Equation (16) confirms the approximate optimality of the scaled $A_{e,r}$ targets in Eq. (15) used by the BCO method [7] for different cruise conditions. Because the approximation errors in Eq. (16) are negligible (see Figs. 2 and 3) when compared to potential inverse design errors for $A_{e,r}$ [7,24], the CFD-based low-boom inverse design optimization using either $A_{e,r}^{target}$ or $A_{e,r}^{opt}$ as the target yields practically the same inverse design optimization solution. So, for the BCO method [7], $A_{e,r}$ of the generated low-boom MDO solution closely matches $A_{e,r}^{target}(\boldsymbol{C}, l_e) \approx A_{e,r}^{opt}(\boldsymbol{C}, l_e)$, where $\boldsymbol{C}$ represents the start of low-boom cruise and l_e is the corresponding effective length. The solution generated by the BCO method has approximately the optimized low-boom shape at the start of low-boom cruise. For example, the CFD-based low-boom inverse design $\widehat{\boldsymbol{D}}_{MaxR}$ in Ref. [7] used the scaling equation [Eq. (15)] to generate $A_{e,r}^{target}(\boldsymbol{C}, l_e)$ from an optimal solution $A_{e,r}^{opt}(\boldsymbol{C}_0, l_{e,0})$ of Eq. (12) for a baseline configuration. The values of μ and δ were fixed at

1.215 and 0.448, respectively. The cruise condition and effective length $(\boldsymbol{C},l_e)$ for $\widehat{\boldsymbol{D}}_{\text{MaxR}}$ had the following values: M = 1.7, H = 52,240 ft, W_{crs} = 133,594 lb, and l_e = 247.4 ft. To compare with $A_{e,r}^{\text{target}}(\boldsymbol{C},l_e)$, the optimal solution $A_{e,r}^{\text{opt}}(\boldsymbol{C},l_e)$ of Eq. (12) is generated for $\widehat{\boldsymbol{D}}_{\text{MaxR}}$. Figure 9 shows that $\widehat{\boldsymbol{D}}_{\text{MaxR}}$ is also an acceptable inverse design using $A_{e,r}^{\text{opt}}(\boldsymbol{C},l_e)$ as the $A_{e,r}$ target and has the potential to attain an undertrack ground noise level of 69.8 PLdB. That is, even though $\widehat{\boldsymbol{D}}_{\text{MaxR}}$ was designed using $A_{e,r}^{\text{target}}(\boldsymbol{C},l_e)$ as the $A_{e,r}$ target, $\widehat{\boldsymbol{D}}_{\text{MaxR}}$ is actually an acceptable inverse design using $A_{e,r}^{\text{opt}}(\boldsymbol{C},l_e)$ as the $A_{e,r}$ target.

IV. Conclusions

Whitham's modified linear theory [8] for steady flow around a supersonic projectile is used to show why the reversed equivalent area $A_{e,r}$ [3] represents an accurate BOR approximation of a low-boom supersonic aircraft for undertrack sonic boom analysis using CFD off-body pressure. This provides the theoretical foundation to an inverse design method for low-boom supersonic aircraft: 1) for the specified design requirements, find the corresponding $A_{e,r}$ target $A_{e,r}^{\text{opt}}$ with the lowest PLdB for undertrack ground signature, and 2) shape a supersonic aircraft such that $A_{e,r}$ of the aircraft equals $A_{e,r}^{\text{opt}}$. Integrating the low-boom inverse design optimization into aircraft conceptual design requires $A_{e,r}^{\text{opt}}$ to vary with the low-boom cruise condition. The $A_{e,r}$ target $A_{e,r}^{\text{opt}}$ is parameterized using the cruise Mach, cruise altitude, cruise weight, effective length, a trim ratio requirement parameter δ, and an a priori estimate μ of $A_{e,r}(l_e)/A_{e,\text{CFD}}(l_e)$ for an expected low-boom design. Numerical results show that the nondimensional form of $A_{e,r}^{\text{opt}}$ is approximately invariant with respect to changes of the cruise condition, provided $\text{PLdB}(A_{e,r}^{\text{opt}}) \leq 70$. As a result, all $A_{e,r}^{\text{opt}}$ with $\text{PLdB}(A_{e,r}^{\text{opt}}) \leq 70$ can be approximately generated by scaling one of them if they have approximately the same effective length and share the same δ and μ. If a supersonic aircraft is an acceptable inverse design for the scaled $A_{e,r}$ target, then it has approximately the optimal low-boom $A_{e,r}$ shape at the low-boom cruise condition when the PLdB value of the undertrack ground signature is the optimization objective.

Acknowledgments

This work is funded by the NASA Commercial Supersonic Technology Project. The author would like to thank James Fenbert at Analytical Mechanics Associates for his constructive comments about this paper.

References

[1] Stevens, S., "Perceived Level of Noise by Mark VII and Decibels (E)," *Journal of the Acoustical Society of America*, Vol. 51, No. 2B, 1972, pp. 575–601. doi:10.1121/1.1912880

[2] Aftosmis, M., Nemec, M., and Cliff, S., "Adjoint-Based Low-Boom Design with Cart3D," AIAA Paper 2011-3500, June 2011. doi:10.2514/6.2011-3500

[3] Li, W., and Rallabhandi, S., "Inverse Design of Low-Boom Supersonic Concepts Using Reversed Equivalent-Area Targets," *Journal of Aircraft*, Vol. 51, No. 1, 2014, pp. 29–36. doi:10.2514/1.C031551

[4] Rallabhandi, S., "Application of Adjoint Methodology to Supersonic Aircraft Design Using Reversed Equivalent Areas," *Journal of Aircraft*, Vol. 51, No. 6, 2014, pp. 1873–1882. doi:10.2514/1.C032518

[5] Wintzer, M., Ordaz, I., and Fenbert, J., "Under-Track CFD-Based Shape Optimization for a Low-Boom Demonstrator Concept," AIAA Paper 2015-2260, June 2015. doi:10.2514/6.2015-2260

[6] Li, W., "Feasibility of Supersonic Aircraft Concepts for Low-Boom and Flight Trim Constraints," AIAA Paper 2015-2581, June 2015. doi:10.2514/6.2015-2581

[7] Li, W., and Geiselhart, K., "Multi-objective, Multidisciplinary Optimization of Low-Boom Supersonic Transports Using Multifidelity Models," *Journal of Aircraft*, Vol. 59, No. 5, 2022, pp. 1137–1151. doi:10.2514/1.C036656.

[8] Whitham, G., "The Flow Pattern of a Supersonic Projectile," *Communications on Pure and Applied Mathematics*, Vol. 5, No. 3, 1952, pp. 301–348. doi:10.1002/cpa.3160050305

[9] Carlson, H., and D. J. Maglieri, D., "Review of Sonic-Boom Generation and Prediction Methods," *Journal of the Acoustical Society of America*, Vol. 51, No. 2C, 1972, pp. 676–685. doi:10.1121/1.1912901

[10] Seebass, R., and George, A., "Sonic Boom Minimization," *Journal of the Acoustical Society of America*, Vol. 51, No. 2C, 1972, pp. 686–694. doi:10.1121/1.1912902

[11] Darden, C., "Minimization of Sonic-Boom Parameters in Real and Isothermal Atmospheres," NASA TN D-7842, March 1975.

[12] Rallabhandi, S., and Mavris, D., "Aircraft Geometry Design and Optimization for Sonic Boom Reduction," *Journal of Aircraft*, Vol. 44, No. 1, 2007, pp. 35–47. doi:10.2514/1.20456

[13] Plotkin, K., Rallabhandi, S., and Li, W., "Generalized Formulation and Extension of Sonic Boom Minimization Theory for Front and Aft Shaping," AIAA Paper 2009-1052, January 2009. doi:10.2514/6.2009-1052

[14] Haas, A., and Kroo, I., "A Multi-Shock Inverse Design Method for Low-Boom Supersonic Aircraft," AIAA Paper 2010-843, June 2010. doi:10.2514/6.2010-843

[15] Morgenstern, J., "Optimum Signature Shaping for Low Sonic Boom," AIAA Paper 2012-3218, June 2012. doi: 10.2514/6.2012-3218
[16] Darden, C., "Sonic-Boom Minimization with Nose-Bluntness Relaxation," NASA TP-1348, January 1979.
[17] Kasuga, Y., and Yoshida, K., "A New F-Function for the Low-Boom Aircraft Design with Trim Requirement," AIAA Paper 2016-2032, January 2016. doi:10.2514/6.2016-2032
[18] Minelli, A., Salah el Din, I., and Carrier, G., "Inverse Design Approach for Low-Boom Supersonic Configurations," *AIAA Journal*, Vol. 52, No. 10, 2014, pp. 2198–2212. doi:10.2514/1.J052834
[19] Park, M., and Carter, M., "Low-Boom Demonstrator Near-Field Summary for the Third AIAA Sonic Boom Prediction Workshop," *Journal of Aircraft*, Vol. 59, No. 3, 2022, pp. 563–577. doi:10.2514/1.C036323
[20] Rallabhandi, S., and Loubeau, A., "Summary of Propagation Cases of the Third AIAA Sonic Boom Prediction Workshop," *Journal of Aircraft*, Vol. 59, No. 3, 2022, pp. 578–594. doi:10.2514/1.C036327
[21] Cleveland, R., Chambers, J., Bass, H., Raspet, R., Blackstock, D., and Hamilton, M., "Comparison of Computer Codes for the Propagation of Sonic Boom Waveforms Through Isothermal Atmospheres," *Journal of the Acoustical Society of America*, Vol. 100, No. 5, 1996, pp. 3017–3027. doi:10.1121/1.417113
[22] Rallabhandi, S., "Advanced Sonic Boom Prediction Using Augmented Burgers Equation," *Journal of Aircraft*, Vol. 48, No. 4, 2011, pp. 1245–1253. doi:10.2514/1.C031248
[23] Ordaz, I., and Li, W., "Approximation of Off-Body Sonic-Boom Analysis for Low-Boom Conceptual Design," *Journal of Aircraft*, Vol. 53, No. 1, 2016, pp. 14–19. doi:10.2514/1.C033159
[24] Li, W., and Geiselhart, K., "Integration of Low-Fidelity MDO and CFD-Based Redesign of Low-Boom Supersonic Transports," *AIAA Journal*, Vol. 59, No. 10, 2021, pp. 3923–3936. doi:10.2514/1.J060368
[25] Morgenstern, J., Norstrud, N., Stelmack, M., and Jha, P., "Advanced Concept Studies for Supersonic Commercial Transports Entering Service in 2030-2035 (N+3)," AIAA Paper 2010-5114, June 2010. doi:10.2514/6.2010-5114
[26] Welge, H., Bonet, J., Magee, T., Tompkins, D., Britt, T., Nelson, C., Miller, G., Stenson, D., Staubach, J., Bala, N., Duge, R., O'Brien, M., Cedoz, R., Barlow, A., Martins, S., Viars, P., Rasheed, A., Kirby, M., Raczynski, C., Roughen, K., Doyle, S., Alston, K., Page, J., and Plotkin, K., "N+3 Advanced Concept Studies for Supersonic Commercial Transport Aircraft Entering Service in the 2030-2035 Period," NASA CR-2011-217084, April 2011.
[27] *U.S. Standard Atmosphere, 1976*, U.S. Government Printing Office, Washington, D.C., 1976. URL: https://www.ngdc.noaa.gov/stp/space-weather/online-publications/miscellaneous/us-standard-atmosphere-1976/us-standard-atmosphere_st76-1562_noaa.pdf [retrieved 2 June 2022].
[28] *Method for Calculation of the Absorption of Sound by the Atmosphere, Annex C*, American National Standards Inst., Standard S1.26-1995, New York, 1995.
[29] *ModelCenter, Version 12.0*, Phoenix Integration Inc., URL:http://www.phoenix-int.com [retrieved 2 June 2022].